

Efficient electrocatalytic CO₂ reduction on a three-phase interface

Jun Li^{1,2}, Guangxu Chen¹, Yangying Zhu¹, Zheng Liang¹, Allen Pei¹, Chun-Lan Wu¹, Hongxia Wang¹, Hye Ryoung Lee³, Kai Liu¹, Steven Chu^{4,5} and Yi Cui^{1,6*}

Electrochemical CO₂ reduction is a critical approach to reducing the globally accelerating CO₂ emission and generating value-added products. Despite great efforts to optimize catalyst activity and selectivity, facilitating the catalyst accessibility to high CO₂ concentrations while maintaining electrode durability remains a significant challenge. Here, we designed a catalytic system that mimics the alveolus structure in mammalian lungs with high gas permeability but very low water diffusibility, enabling an array of three-phase catalytic interfaces. Flexible, hydrophobic, nanoporous polyethylene membranes with high gas permeability were used to enable efficient CO₂ access and a high local alkalinity on the catalyst surface at different CO₂ flow rates. Such an alveolus-mimicking structure generates a high CO production Faradaic efficiency of 92% and excellent geometric current densities of CO production (25.5 mA cm⁻²) at -0.6 V versus the reversible hydrogen electrode, with a very thin catalyst thickness of 20–80 nm.

The electrochemical carbon dioxide reduction reaction (CO₂RR) has attracted great research interest as a carbon neutral route for a renewable energy future^{1–3}. Competing with the dominant electrochemical water reduction to H₂ in aqueous solutions—also known as the hydrogen evolution reaction (HER)⁴—the multi-proton and multi-electron CO₂RR pathways are kinetically sluggish and require excessive reducing potentials⁵. Substantial efforts have been invested in developing heterogeneous electrocatalysts with enhanced CO₂RR activities, including metals^{6–9} (for example, Au, Cu, Ag, Pd and Sn), metal oxides^{10,11} and chalcogenides¹², and carbon-based materials¹³, particularly focusing on the optimization of their catalytic performances by tailoring particle morphology^{14,15}, size¹⁶, thickness¹⁷, grain-boundary¹⁸ and defect density^{19–21}.

In contrast, the accessibility of the catalyst to high concentrations of CO₂ molecules is critical, but generally deficient. The challenge is that the ratio of CO₂ to H₂O molecules in an aqueous solution is only ~1:1,300 at 1 atm pressure. Increasing the CO₂ concentration by increasing the pressure has a limited effect and introduces a non-trivial constraint for practical applications. Gas diffusion layers (GDLs)—typically formed from polytetrafluoroethylene (PTFE)-treated porous carbon membranes—are widely applied to enhance gas transport to the electrochemical interface, such as that in fuel cells²² and CO₂ electrocatalysis^{23,24}. However, excessive electrolyte contact over extended use tends to reduce the hydrophobicity of a GDL, which is known as flooding, thus hindering the mass transport and resulting in poor durability and degradation^{25–29}. Alkaline metal ion-mediated adsorption was explored to increase the CO₂ concentration at the catalyst surface, but the effect was limited by solubility of the relevant salts³⁰. High pH electrolytes were reported to achieve higher current densities than those in close-to-neutral pH electrolytes (for example, 0.5 M KHCO₃)²³, whereas the high alkalinity inevitably results in a significant reaction with CO₂, thus requiring a constant flow of the high-alkaline electrolyte to

compensate for the reaction loss (Supplementary Fig. 1a)^{31–34}. Recently, a high local electric field at gold nanotips was shown to enhance local CO₂ concentrations³⁵, resulting in a high current density of conversion to CO (1.1 mA cm⁻², based on the electrochemical active surface area (ECSA)) with excellent selectivity, which indicates the importance of the catalyst's access to the high CO₂ concentration. Above all, we believe that significant opportunities exist for redesigning electrode structures to directly deliver high concentrations of gas phase CO₂ molecules to the catalyst surface with minimum alkaline consumption, which requires the efficient three-phase contact of CO₂ (gas), H₂O (liquid) and catalyst (solid) for the electrochemical CO₂RR.

Thus, we propose a design strategy that mimics a mammalian lung—an efficient biological system for delivering O₂ from the air outside the human body to the blood stream. The alveolus—the most basic unit of a mammalian lung (Fig. 1a, left)—is an evolutionarily engineered compartment of around 200 μm in diameter enclosed by several ultrathin epithelial cellular membranes (~1 μm thick) with high gas permeability but very low water diffusibility^{36,37}. O₂ is transported by gas flow during the inhalation process from macroscopic tubes (bronchioles) into microscopic alveoli. During human pulmonary circulation, gases can rapidly penetrate these multilayered membranes to be exchanged between the alveoli and blood capillaries, while liquids stay separated (Fig. 1a, right). Haemoglobin proteins in the red blood cells function as catalysts by capturing and binding with O₂. CO₂ released from the blood to outside the body follows the opposite path. Essentially, a lung is a sophisticated system engineered by nature that consists of bicontinuous interpenetrating networks of gas and liquid phases separated by a thin, gas-permeable, but waterproof membrane with enzyme catalysts in the blood capillaries at very short distances from the membrane.

Based on the working mechanism of the alveolus, we developed a bilayer pouch-type artificial alveolus structure (Fig. 1b–f),

¹Department of Materials Science and Engineering, Stanford University, Stanford, CA, USA. ²Department of Chemistry, Stanford University, Stanford, CA, USA. ³Department of Electrical Engineering, Stanford University, Stanford, CA, USA. ⁴Department of Physics, Stanford University, Stanford, CA, USA. ⁵Department of Molecular and Cellular Physiology, Stanford University, Stanford, CA, USA. ⁶Stanford Institute for Materials and Energy Sciences, SLAC National Accelerator Laboratory, Menlo Park, CA, USA. *e-mail: yicui@stanford.edu

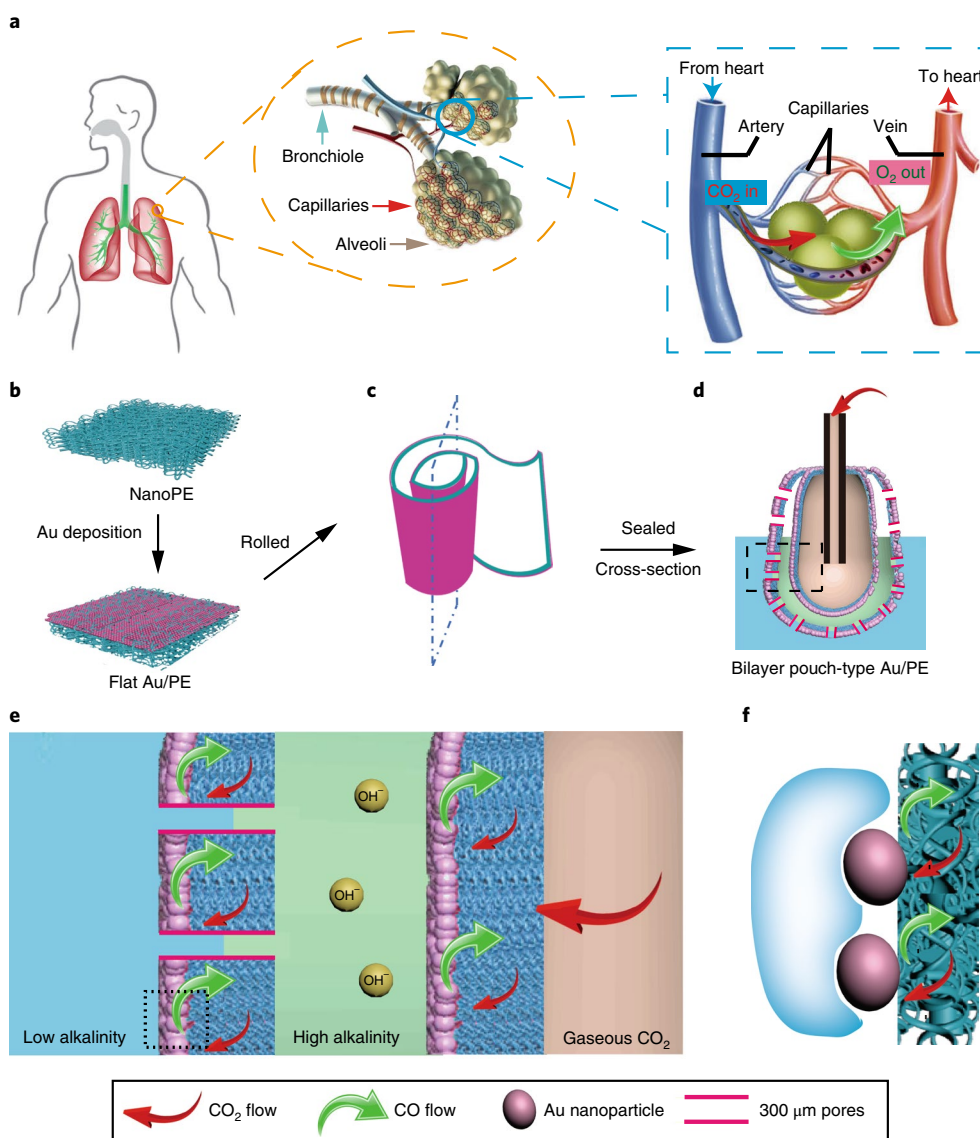


Fig. 1 | Schematics of the artificial lung-inspired Au/PE catalyst system for efficient electrocatalytic CO₂ reduction. **a**, Illustrations of the human lung, alveoli and CO₂/O₂ exchange in pulmonary circulation. **b**, Schematic of a flat Au/PE membrane prepared by sputtering a layer of gold nanoparticles on one side of the polyethylene membrane surface. **c**, Schematic of rolling a piece of flat Au/PE membrane into a bilayer structure. The bottom and top edges of the rolled Au/PE membrane are further sealed to form a closed pouch-type structure mimicking a human alveolus. **d**, Cross-section illustration of a bilayer pouch-type Au/PE structure, where CO₂ gas is delivered to the central compartment that is separated from the external electrolyte by the water-impenetrable nanoPE membrane. **e**, More detailed image (dashed line in **d**) of the bilayer structure consisting of the inner gaseous CO₂ (brown), high-alkalinity interlayer electrolyte (green) and low-alkalinity bulk electrolyte (blue). Ions in the electrolyte are transferred through pinholes on the outer polyethylene membrane. **f**, More detailed image (dotted line in **e**) of the three-phase interface between the Au/H₂O/CO₂.

which is constructed from a highly flexible nanoporous polyethylene (nanoPE) membrane sputtered with a layer of gold nanocatalyst on one side. With the hydrophobic property of nanoPE, this artificial alveolus structure can offer a large number of catalytic active sites at the three-phase interface and achieve local pH tuning in the pouch. Benefiting from this design for the electrochemical CO₂RR, an excellent Faradaic efficiency to CO production (FE_{CO}) of ~92% and a high geometric current density for CO production of ~25.5 mA cm⁻² were achieved for the electrochemical CO₂RR at -0.6 V versus the reversible hydrogen electrode (RHE).

Results

Fabrication and characterization of the electrode. To fabricate the bilayer pouch-type artificial alveolus structure, gold nanoparticles ~20 nm in size were first deposited onto one side of a 12-μm-thick

flexible, hydrophobic nanoPE membrane (designated as flat Au/PE; Fig. 1b) by magnetron sputtering (characterized by scanning electron microscopy (SEM) in Fig. 2b and Supplementary Fig. 2, and X-ray diffraction in Supplementary Fig. 3; see Methods). Such nanoPE can be mass-produced in a roll-to-roll fashion at an extremely low cost (~US\$1 per m²)³⁸ and features interconnected fibres with a collection of pore radius sizes ranging from 40 to 500 nm (Fig. 2a). The hydrophobic and nanoporous nature of nanoPE makes it impermeable to water but allows gas diffusion. Gold was chosen as a model catalyst as it can catalyse the electrochemical reduction of CO₂ to CO (ref. 17). To mimic the closed alveolus with bronchioles for gas transport in and out of a mammalian lung, the flat Au/PE membrane was then rolled (Fig. 1c) and sealed to form a single-layered (Supplementary Fig. 1b) or bilayer pouch-type structure (Fig. 1d and Supplementary Fig. 1c). In the

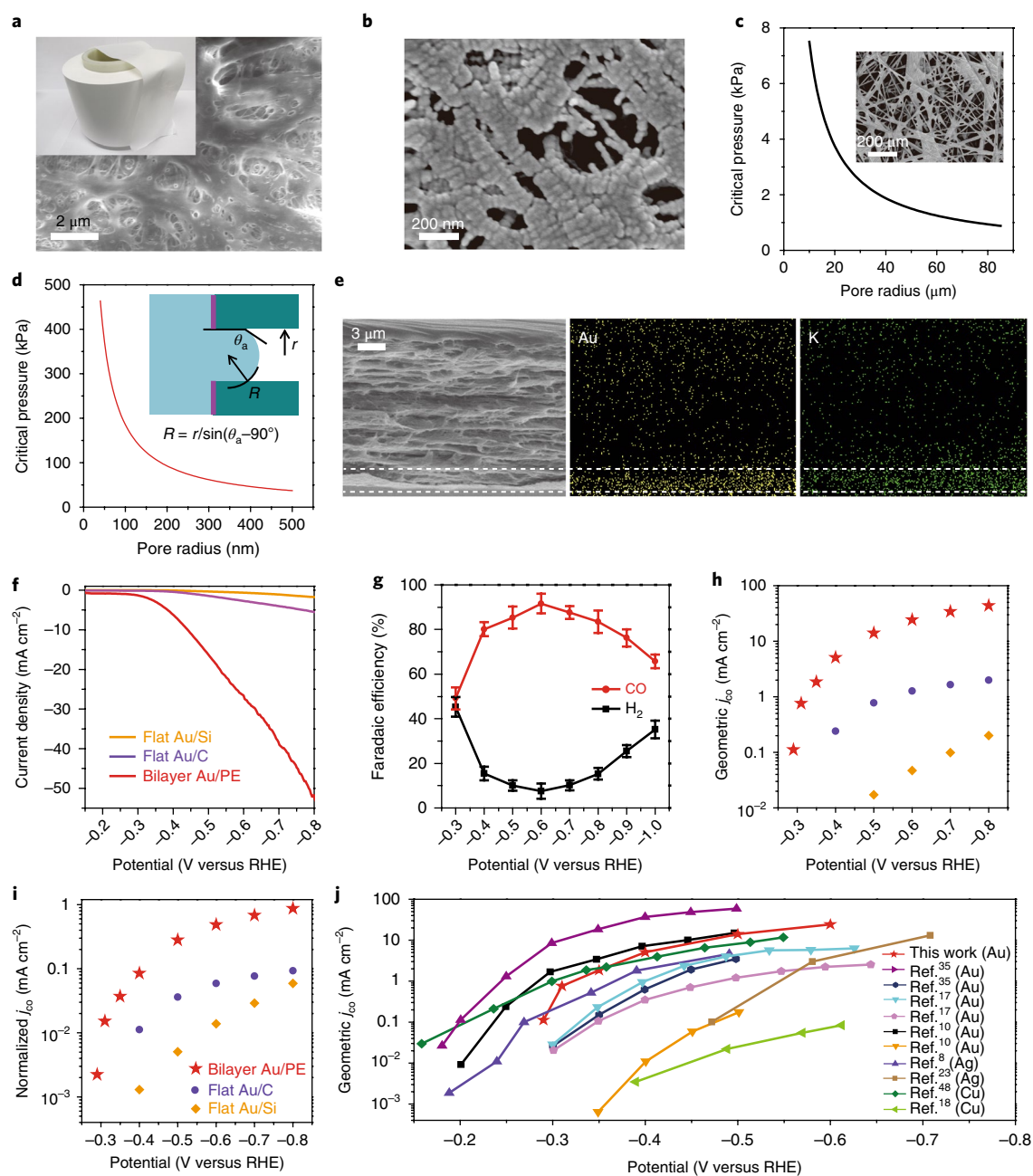


Fig. 2 | Structural characterizations and electrocatalytic CO_2 reduction performances of the Au/PE membranes. **a**, SEM image and (inset) photograph of a pristine nanoPE membrane. **b**, SEM image of a gold-coated polyethylene membrane. **c**, Critical burst-through pressure for a carbon-based GDL as a function of its pore radius. Inset: SEM image of the carbon-based GDL. **d**, Critical burst-through pressure for the nanoPE membrane as a function of its pore radius, r . Inset: schematic of the liquid-vapour interface advancing inside the pore with an advancing contact angle θ_a greater than 90° . **e**, Energy-dispersive X-ray spectroscopy mapping of the cross-section of an Au/PE membrane after a 24 h electrochemical test in a K^+ -containing electrolyte. The high-density dotted area (between the two marked white dashed lines) shows the location of the gold and potassium elements. The sparsely distributed dots are noise signals. **f**, LSV curves of a bilayer pouch-type Au/PE membrane (red curve), flat Au/C (purple curve) and flat Au/Si (yellow curve) in CO_2 -saturated 0.5 M $KHCO_3$. **g**, Faradaic efficiencies of CO (red curve) and H_2 production (black curve) by a bilayer pouch-type Au/PE. The error bars represent the standard deviation of three independent samples. **h**, **i**, Geometric (**h**) and normalized (**i**) current densities of CO production for a bilayer pouch-type Au/PE (red stars), flat Au/C (purple circles) and flat Au/Si (yellow diamonds). **j**, Activity of various CO_2 reduction catalysts based on the partial current densities for CO production at variable potentials. Data were derived from refs. 8,10,17,18,23,35,48.

bilayer pouch-type structure, the central sealed compartment was separated from the external electrolyte by the water-impenetrable nanoPE membrane and connected to one inlet for CO_2 to flow in, from which CO_2 can diffuse into the pores of the nanoPE membrane and subsequently throughout the whole nanoporous framework. To enable ion exchange between the interlayer electrolyte and

external bulk electrolyte, several pinholes with $\sim 300 \mu m$ diameters were punched on the outer layer (Fig. 1e). The detailed fabrication process and experimental set-up are displayed in the Methods and Supplementary Fig. 4. Due to the internal pressure induced by CO_2 in an enclosed environment, and the strongly hydrophobic and nanoporous structure of nanoPE, the electrolyte can wet the gold

catalyst surface but not the polyethylene or nanopores, which allows CO₂ gas to diffuse in the plane of the nanoPE membrane to make contact with the gold and water directly, forming an array of robust and efficient three-phase contact interfaces between the gold, H₂O and CO₂ for the CO₂RR (Fig. 1f). In contrast, a conventional flat structure surrounded by the electrolyte can only utilize the CO₂ dissolved in the electrolyte, which results in insufficient three-phase contact interfaces and subsequently lower activity and selectivity (Supplementary Fig. 1d). For comparison, we also prepared gold deposited on the PTFE-coated carbon paper (Toray TGP-H-060) and the silicon wafer (designated as Au/C and Au/Si, respectively) using the same sputtering method, and their surface morphologies were also characterized by SEM (Supplementary Fig. 5a–d).

Calculations of the anti-flooding capability of the electrode.

To illustrate the robustness of our Au/PE membrane in maintaining the three-phase contact in an aqueous solution, a theoretical model was first applied to calculate the gas–liquid–solid three-phase contact line position of the Au/PE membrane compared with gold on the PTFE-coated porous carbon typically used for the GDL (Supplementary Note 1). For a carbon-based GDL, the critical burst-through pressure was calculated as ~0.88 kPa for its largest pore radius of ~85 µm (Fig. 2c). This relatively low burst-through pressure is consistent with the previous observation of water flooding of the GDLs^{29,39,40}, which may be due to the relatively larger pore size²⁵, carbon corrosion⁴¹ and the imperfect PTFE coating^{26,29,42,43}. In contrast, the nanoPE membrane presents a homogeneous surface composition and much smaller pore sizes. The critical burst-through pressure of the nanoPE was calculated as ~37 kPa (about 42 times higher than that of a GDL), even for its largest pore radius size of 500 nm (Fig. 2d and inset), which indicates that liquid does not flood the nanoPE membrane.

In addition, the contact angle measurements were conducted to compare the hydrophobicity change of the Au/PE membrane and Au/carbon-based GDL after 24 h of continuous electrochemical testing under –1.0 V using an electrochemical reactor developed in previous work⁴⁴. The contact angle on the gas phase side of the Au/carbon-based GDL significantly decreased from 148 to 119° (Supplementary Fig. 6a,b), whereas the contact angle on the gas phase side of the nanoPE underwent a much smaller change (decreasing from 109 to 105°; Supplementary Fig. 6c,d), indicating that the Au/PE membrane is much more stable than the Au/carbon-based GDL. Energy-dispersive X-ray spectroscopy mapping characterization of the Au/PE membrane after 24 h of electrochemical testing in a K⁺-containing electrolyte showed that the electrolyte can only wet the same depth as the gold layer thickness for the Au/PE (Fig. 2e), whereas K⁺ penetrates through the Au/carbon-based GDL under similar conditions (Supplementary Fig. 7), further confirming the robustness of the Au/PE three-phase interface after long-term use. Moreover, due to its ultrathin thickness (12 µm; cross-section SEM in Supplementary Fig. 8a), the nanoPE is super-flexible and can be rolled to form single- or bi-layered pouch-type structures with a bending diameter even less than 1 mm without cracking (Supplementary Fig. 8b), significantly surpassing the thinnest flexible commercial carbon-based GDL with a thickness of ~300 µm (Supplementary Fig. 8c,d).

Electrocatalytic performances. The electrochemical CO₂ reduction activities of Au/PE membranes were investigated in an H-type electrochemical cell⁴⁵ separated by a cation exchange membrane with CO₂-saturated 0.5 M KHCO₃ as the electrolyte (Methods). Au/C and Au/Si deposited with a similar thickness of gold were also tested for comparison. Linear sweep voltammetry (LSV) curves showed that the bilayer Au/PE membrane exhibits the best performance among these samples (Fig. 2f). As the initially stabilized current density varied slightly due to capacitive current,

the onset potential was defined as the potential at which the current density was 0.2 mA cm^{–2} higher than the initially stabilized current density of each sample in our work. In this work, the potentials reported are all converted into RHE. The onset potentials and overpotentials for the bilayer Au/PE, flat Au/C and flat Au/Si electrodes are listed in Supplementary Table 1. The bilayer Au/PE membrane exhibited the lowest onset potential of –0.27 V (corresponding to 160 mV overpotential for CO₂/CO) and the highest total geometric current densities (j_{tot}) at different applied potentials. For instance, at –0.6 V, the j_{tot} values of Au/PE, Au/C and Au/Si were –26.6, –2.7 and –0.6 mA cm^{–2}, respectively.

The electrochemical reduction products were then examined by applying several fixed potentials between –0.3 and –1.0 V, during which the gas products were periodically sampled and quantified by on-line gas chromatography. In our system, CO and H₂ were the two dominant products, together with an overall Faradaic efficiency larger than 95%. More importantly, the bilayer Au/PE membrane exhibited much higher Faradaic efficiencies for CO₂ reduction to CO than H₂ generation in the whole voltage range from –0.4 to –1.0 V, with the highest FE_{CO} value of ~92% at –0.6 V (Fig. 2g). In contrast, Au/C and Au/Si showed substantially higher Faradaic efficiencies for H₂ generation and lower FE_{CO} values of <60% and <20%, respectively, in the whole voltage window tested (Supplementary Fig. 9). In addition, at a fixed layer spacing of 1 mm, the FE_{CO} values at –0.6 V of different layered Au/PE samples were compared. FE_{CO} first increased with increasing layer numbers from a flat membrane to a bilayer pouch with a peak value of ~92%. It then decreased to a tri-layered pouch (Supplementary Fig. 10).

The CO₂ reduction activities of different catalysts were further examined with respect to their geometric surface areas (that is, geometric j_{CO} ; Fig. 2h) and ECSAs (that is, normalized j_{CO} ; Fig. 2i). The ECSAs were measured by an oxygen monolayer chemisorption method^{46,47}, and the electrochemical roughness factors (defined as the ratio between the ECSA and geometric surface area) of these catalysts were calculated (Supplementary Fig. 11 and Supplementary Table 2)³⁵. The bilayer Au/PE presented the highest CO production reactivity in both geometric j_{CO} and normalized j_{CO} values compared with those of Au/C and Au/Si, indicating a much higher catalytic activity per electrochemically reactive site. To show that CO₂ is indeed efficiently transported through, and in the plane of the polyethylene membrane, we compared the activity and selectivity of the flat structure, single-layered structure and bilayer with only the outer layer coated structure (designated as the bilayer-outer layer coating) (Supplementary Fig. 12). Both the single-layered structure and bilayer-outer layer coating clearly showed enhanced current densities and FE_{CO} values compared with those of the flat structure. Our data indicate that the polyethylene membrane can efficiently enhance the mass transport of a gaseous CO₂ feed towards the electrocatalyst surface.

To emphasize the significance of our alveolus-inspired catalyst design for CO₂ access and reduction, the CO₂RR current density normalized by the geometric surface area (that is, geometric j_{CO}) of the bilayer Au/PE membrane was further plotted, along with the results from recent representative literature^{8,10,17,18,23,35,48} (Fig. 2j). Our current density represents one of the highest values reported to date using an H-cell electrochemical set-up⁴⁸, which is highly remarkable given the ultrathin catalyst loading (Supplementary Table 3; all tested in 0.5 M KHCO₃). This comparison can be further highlighted by plotting the saturated normalized current densities with different catalyst layer thicknesses in the literature (Supplementary Fig. 13). Considering the total gold thickness on a bilayer polyethylene membrane, the gold catalyst loading was 0.154 mg cm^{–2}, which was about 8–10% of the average loadings in other works (typically 1–2 mg cm^{–2}). The thickness of the porous catalyst layer used in GDL-based electrodes is even larger and typically in the range of 5–20 µm (ref. 49). Despite the much thinner thickness of the gold

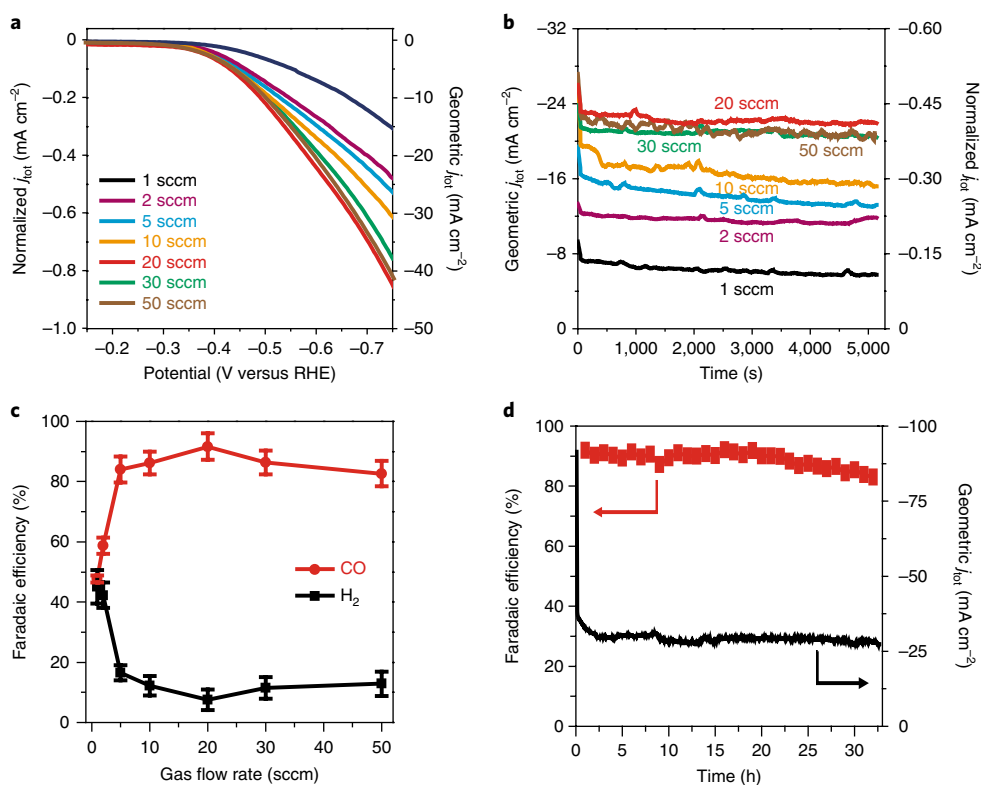


Fig. 3 | Electrocatalytic performances under different CO₂ flow rates. **a–c**, LSV curves (**a**), time-dependent total current densities at -0.6 V (**b**) and corresponding Faradaic efficiencies (**c**) of a bilayer pouch-type Au/PE membrane under different CO₂ flow rates. The error bars in **c** represent the standard deviation of three independent samples. **d**, Time-dependent total current density at -0.6 V and FE_{CO} of a bilayer pouch-type Au/PE membrane.

catalyst (that is, 20–80 nm in this work versus several μm in other work), our bilayer Au/PE achieves a high saturated normalized current density of 1.0 mA cm^{-2} at -0.8 V, which exceeds that of most other catalysts with much larger catalyst thicknesses and is comparable to the record performances of gold nanoneedles with $\sim 100\times$ greater thicknesses³⁵ (Supplementary Fig. 13). This exceptional performance indicates that the improved access of the catalyst to CO₂ through increased CO₂ permeability of the alveolus-mimicking Au/PE leads to higher intrinsic CO₂RR activities.

The distinctive feature of the high CO₂ permeability across Au/PE membranes was further demonstrated by measuring electrocatalysis at different CO₂ gas flow rates. Normally, an increase of the CO₂ concentration around the catalyst surface leads to an increase of both the CO₂RR conversion yield and selectivity, and previous reports have shown that much higher CO₂ partial pressures and concentrations are needed to achieve FE_{CO} saturation^{10,48,50}. Nonetheless, a striking difference was observed for the bilayer Au/PE membrane. The overall geometric current density of the bilayer Au/PE membrane was continually enhanced with increasing CO₂ flow rates from 1 to 20 standard cubic centimetres per minute (sccm), and saturated at higher flow rates of 30 and 50 sccm (Fig. 3a,b). However, the corresponding FE_{CO} value quickly increased with the CO₂ flow rate from 1 to 5 sccm, reached a plateau of $>85\%$ at 5 sccm and remained high at larger flow rates (Fig. 3c), significantly differing from previous reports⁴⁸. This unique characteristic of FE_{CO} saturation at low CO₂ flow rates is attributed to the nanoporous surface feature of the Au/PE membrane, which allows for extremely efficient gas permeability and exchange, similar to an alveolus for gas exchange. For the flat Au/C structure, the overall geometric current density did not change much above 5 sccm, indicating less activity for the flat Au/C structure (Supplementary Fig. 14). Moreover, the electrochemical stability of the bilayer Au/PE membrane was evaluated at a constant -0.6 V in CO₂-saturated

0.5 M KHCO₃ (Fig. 3d). Except for a quick drop of current density in the first several minutes, the current density was well maintained for over 35 h. The FE_{CO} value was also well maintained during the whole process with only a slight decay from 92 to 80%. In addition, no flooding was observed in the Au/PE membrane after 35 h of continuous electrochemical testing, indicating the excellent stability of this system.

The observation that our bilayer Au/PE architecture outperforms the flat nanoPE and the carbon-based GDL architecture in a close-to-neutral solution (for example, CO₂-saturated 0.5 M KHCO₃) can be explained by the increased alkalinity between different layers of a bilayer Au/PE (Fig. 1e). Previous theoretical calculations indicated that both CO₂RR and HER processes lead to an increase of alkalinity near the electrode/catalyst surface^{51,52}, and the local pH can be up to 6 units higher than the bulk pH⁵¹ (see also Supplementary Note 2 for a demonstration of solution alkaline increases). The increased surface pH, in turn, restricts the availability of protons on the surface and significantly inhibits the HER activity, thereby increasing the number of active sites available for the CO₂RR^{23,33–55}. In addition, a high pH is also beneficial for the activation of CO₂ in solution²⁸. However, under conventional conditions, such as in H-type electrochemical cells, this proton depletion condition, which improves the CO₂RR selectivity over HER, is difficult to maintain due to strong turbulence-induced stirring effects for CO₂ transport to and from the catalyst surface^{17,51}. Though increasing the alkalinity of the bulk solution (such as by using 3 M KOH) can also provide a high current density²³, this KOH bulk solution can substantially react with CO₂, reducing the available CO₂ concentration and decreasing the solution pH gradually^{31,56,57}. Hence, the GDL-based flow reactor requires constantly flowing KOH electrolytes to compensate for the reaction loss (Supplementary Fig. 1a)^{23,31–34}, which inevitably consumes a large amount of CO₂ reactant and alkaline electrolyte; thus, it is economically unfavourable in the future scale-up stage²⁸.

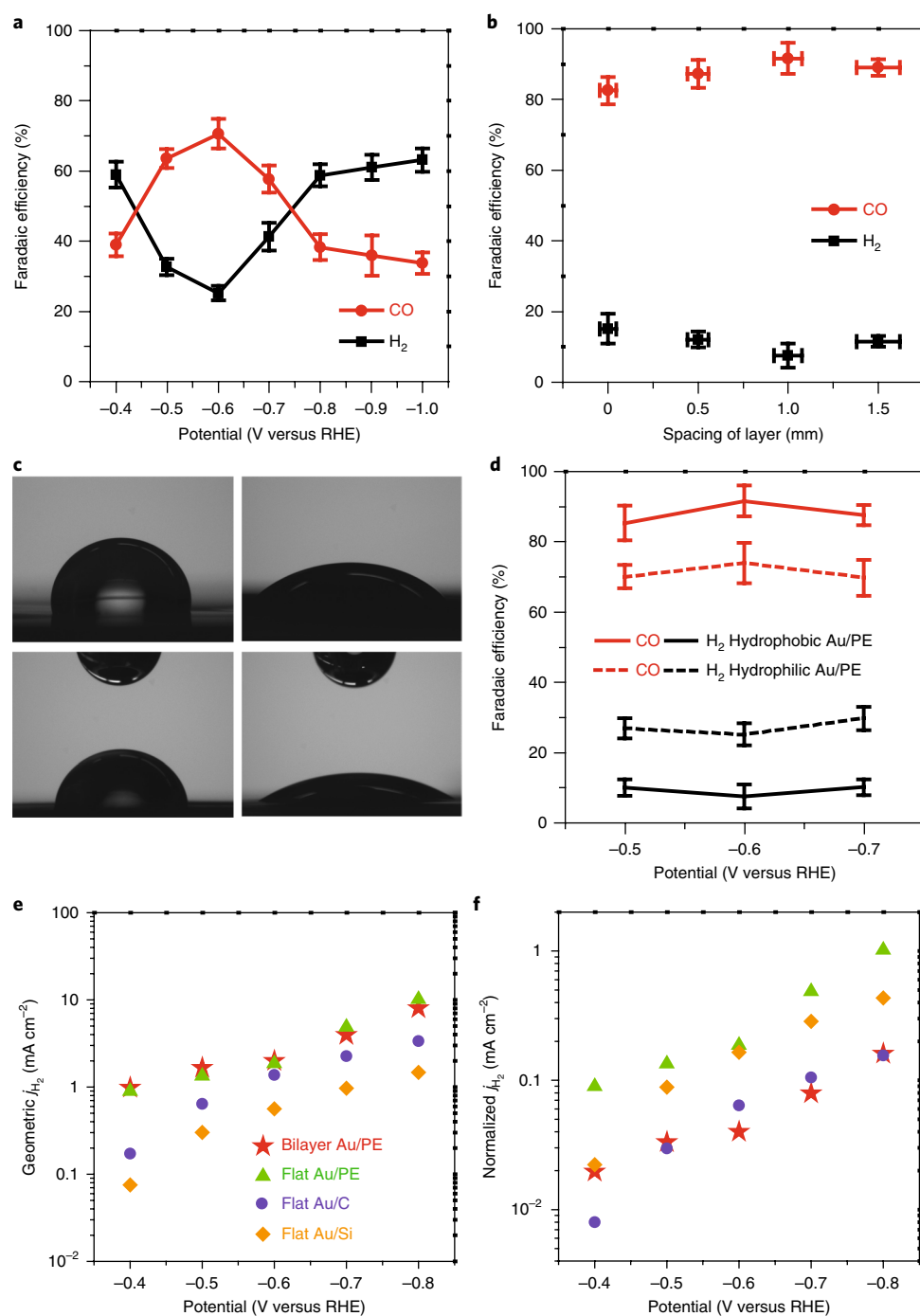


Fig. 4 | Performance comparison of different Au/PE membranes for CO₂ and water reduction. **a**, Faradaic efficiencies of CO (red curve) and H₂ formation (black curve) from flat Au/PE membranes. The error bars represent the standard deviation of three independent samples. **b**, Dependence of Faradaic efficiencies of bilayer pouch-type Au/PE membranes on the layer spacing. The error bars represent the standard deviation of three independent samples. **c**, Photographs of contact angles on pristine hydrophobic nanoPE (top left), pristine hydrophobic Au/PE (bottom left), plasma-treated hydrophilic nanoPE (top right) and plasma-treated hydrophilic Au/PE (bottom right). **d**, Faradaic efficiencies of CO and H₂ production of hydrophobic (solid lines) and hydrophilic bilayer Au/PE pouch-type membranes (dotted lines). The error bars represent the standard deviation of three independent samples. **e,f**, Geometric (**e**) and normalized (**f**) current densities of H₂ production for bilayer pouch-type Au/PE (red stars), flat Au/PE (green triangles), flat Au/C (purple circles) and flat Au/Si (yellow diamonds).

In addition to the abundant and catalytically stable active sites at the three-phase interface, a higher pH value can also be well controlled in the interlayer of our bilayer Au/PE structure (Fig. 1e). We measured the change of the local pH in the interlayer and plotted the pH over time (Supplementary Fig. 15a), which shows that the pH increased within the first 50 min and reached a plateau of

~9.6, suggesting that the bicarbonate/carbonate/CO₂(aq) eventually reached a steady state in the interlayer. Further increase of this local pH was inhibited by the slow but continuous charge transport of the bulk buffer through the holes on the outer polyethylene membrane. This result was also consistent with previous theoretical calculations (Supplementary Fig. 15b) and our phenolphthalein test

(Supplementary Note 2). No excessive flowing of high-alkalinity electrolyte was needed, which is distinctively different from a GDL-based electrode (Supplementary Fig. 1a). Thus, the superior CO₂RR performance on the bilayer Au/PE structure is attributed to the synergistic effect of the three-phase interface and high local pH at the active sites.

To demonstrate the effect of each layer in the bilayer pouch-type structure Au/PE, the total current densities and Faradaic efficiencies of four samples (fabrication process in Supplementary Fig. 16) were measured. Among these metal-coated pouch-like nanoPE membranes, the bilayer Au/PE achieved the best total current density and FE_{CO} (Supplementary Fig. 17). Further increasing the catalyst loading of the flat Au/PE structure to the same geometry catalyst loading of the bilayer Au/PE (that is, 0.154 mg cm⁻²) only negligibly improved the electrochemical performance (Supplementary Fig. 18). These results indicate that the inner layer contributes to most of the CO₂RR catalytic reaction due to the local high pH and three-phase interfaces. The outer layer is indispensable to the retention of local high pH in the interlayer and contributes some CO₂-to-CO partial current density. Thus, the bilayer (that is, with inner and outer layers together) can achieve the highest activity and selectivity in a near-neutral bulk electrolyte.

The dependence of the bilayer Au/PE membrane performance on the nanoPE layer spacing was further studied. With a bilayer Au/PE structure, an optimal FE_{CO} was achieved with a layer spacing of ~1 mm (Fig. 4b). The optimization of the layer spacing allows for effective enhancement of CO₂ transport and adsorption, while at the same time reducing water diffusion between the interspacing of nanoPE membranes and the bulk electrolyte. Moreover, both pristine polyethylene and Au/PE membranes showed large contact angles of 109 and 83° (Fig. 4c), indicating their hydrophobic and slightly hydrophilic surfaces. After hydrophilic treatment with plasma, the contact angles were substantially reduced to 46 and 36°, respectively. Hydrophilic treatment of the Au/PE membrane led to a clear increase of the HER and a corresponding decrease of the CO₂RR (Fig. 4d), indicating the loss of selective gas-versus-liquid permeability.

Finally, the geometric and normalized current densities of HER (j_{H_2}) are plotted for these catalysts. Though the geometric j_{H_2} plot shows that the bilayer Au/PE has a similar current density to the flat Au/PE structure for H₂ production (Fig. 4e), the normalized j_{H_2} of the bilayer Au/PE membrane is about one order of magnitude lower than that of the flat Au/PE, and also lower than that of both Au/C and Au/Si (Fig. 4f). This substantially depressed j_{H_2} indicates that only a small proportion of its ECSA contributes to H₂ production, possibly due to the inhibition of OH⁻ diffusion and subsequent depletion of protons inside the bilayer structures. Taken together, the normalized j_{CO} and j_{H_2} clearly represent the corresponding activities of a unit gold catalytic site, and as such, the bilayer Au/PE presents the highest CO₂RR activity but the lowest HER activity.

To elucidate the artificial alveolus (bilayer pouch-type) electrode structural superiority to a conventional flat electrode structure, we chose a facile sputtering method to directly deposit polycrystalline gold nanoparticles on different substrates that initially do not show high activity or selectivity for CO production, as indicated in previous work^{10,16,35}, as well as our control samples of flat Au/PE, Au/C and Au/Si. In contrast, the bilayer Au/PE architecture achieved a high CO production selectivity of ~92% Faradaic efficiency and excellent geometric current densities of CO production (~25.5 mA cm⁻²) at -0.6 V, with a very thin catalyst thickness of 20–80 nm. Another unique feature of our design is the capability to switch between a conventional flat electrode structure and an alveolus-mimicking bilayer pouch-type Au/PE architecture that contacts with one gas phase and two electrolytes of different alkalinities, thus enabling a direct and unambiguous comparison and

key structure–activity insights into these two structures using the same catalyst.

Conclusion

In summary, the bilayer, hydrophobic, nanoporous Au/PE membrane represents a simple but highly effective artificial alveolus structure for the CO₂RR. The interconnected nanopores of the hydrophobic polyethylene membrane enable efficient CO₂ delivery with a high flux, but inhibit water penetration, mimicking the alveolus membrane. A local pH increase is also achieved, which further enhances the electrocatalytic reduction of CO₂ while suppressing the reduction of H₂O. Such an artificial alveolus design maximizes the efficiency of the three-phase contact (CO₂ gas, solid catalyst and liquid electrolyte), thereby featuring excellent CO₂ reduction activity performances even with much lower catalyst loadings.

Methods

Fabrication of flat Au/PE membranes. A piece of nanoPE membrane (Teklon, 12 μm thick; Entek International) was cut to a suitable size (for example, 10 cm × 10 cm). A thin gold layer was then directly deposited by d.c. magnetron sputtering (AJA International) of a gold target (99.99%; Alfa Aesar) on the nanoPE membrane at an applied power of 150 W and a working pressure of 10 mTorr for 2 min under an argon atmosphere (99.9995%; Air Liquide). The thickness of the obtained gold film was ~20 nm (corresponding to 0.0386 mg cm⁻²). To obtain a flat Au/PE membrane with a mass loading of 0.154 mg cm⁻², the sputter time was extended to 8 min. The fabrication of the bilayer pouch-type Au/PE membrane is described in Supplementary Fig. 4.

Hydrophilic treatment of the polyethylene and Au/PE membranes. The hydrophilic Au/PE membranes were prepared by treating pristine Au/PE membranes with oxygen plasma (Evactron Decontaminator; XEI Scientific), with 400 mTorr of O₂ at 14 W for 3 min. The contact angle measurements were conducted in a contact angle goniometer (ramé-hart 290).

Electrochemical measurements. All the electrochemical experiments were conducted at 25 °C in an H-type electrochemical cell separated by a selenion anion exchange membrane. Each chamber contained 25 ml of electrolyte (for example, CO₂-saturated 0.5 M KHCO₃), which was stirred at a constant rate of 300 r.p.m. A carbon rod was used as the counter electrode in the anode side of the chamber. Both the working and reference electrodes were put into the cathode side of the chamber. A 16-channel potentiostat (VMP3; Bio-Logic Science Instruments) was used for all electrochemical experiments. All potentials were measured against a saturated calomel reference electrode (SCE) and converted to the RHE reference using:

$$E \text{ (versus RHE)} = E \text{ (versus SCE)} + 0.240 \text{ V} + 0.0591 \text{ V} \times \text{pH}. \quad (1)$$

CO₂ reduction electrolysis and product analysis. The catholyte was pre-saturated with CO₂ by continuously purging with 50 sccm CO₂. The positions of the gaseous CO₂ inlet for different polyethylene structures during the electrochemical testing are shown in Supplementary Fig. 1b–d. The working compartment was directly connected to an on-line gas chromatography instrument (8610C; SRI Instruments) equipped with a molecular sieve 13× capillary column, thermal conductivity detector and flame ionization detector to analyse the evolved gaseous products. Argon (99.9995%; Air Liquide) was used as the carrier gas. The partial current densities of CO and H₂ production were calculated from the gas chromatograph peak areas as:

$$j_{CO} = \frac{\text{peak area}}{\alpha} \times \text{flow rate} \times \frac{2Fp_0}{RT} \times (\text{electrode area})^{-1} \quad (2)$$

$$j_{H_2} = \frac{\text{peak area}}{\beta} \times \text{flow rate} \times \frac{2Fp_0}{RT} \times (\text{electrode area})^{-1} \quad (3)$$

where α and β are conversion factors for CO and H₂, respectively, based on the calibration of the gas chromatograph with a standard sample, $p_0 = 1.013$ bar, T is the temperature, F is the Faradaic constant and R is the gas constant.

Data availability. The data that support the plots within this paper and other finding of this study are available from the corresponding author upon reasonable request.

Received: 31 October 2017; Accepted: 15 June 2018;
Published online: 23 July 2018

References

- McDonald, T. M. et al. Cooperative insertion of CO₂ in diamine-appended metal-organic frameworks. *Nature* **519**, 303–308 (2015).
- Liu, C., Colón, B. C., Ziesack, M., Silver, P. A. & Nocera, D. G. Water splitting-biosynthetic system with CO₂ reduction efficiencies exceeding photosynthesis. *Science* **352**, 1210–1213 (2016).
- Mistry, H., Varela, A. S., Köhl, S., Strasser, P. & Cuenya, B. R. Nanostructured electrocatalysts with tunable activity and selectivity. *Nat. Rev. Mater.* **1**, 16009 (2016).
- Cabán-Acevedo, M. et al. Efficient hydrogen evolution catalysis using ternary pyrite-type cobalt phosphosulphide. *Nat. Mater.* **14**, 1245–1251 (2015).
- Liu, C. et al. Nanowire-bacteria hybrids for unassisted solar carbon dioxide fixation to value-added chemicals. *Nano Lett.* **15**, 3634–3639 (2015).
- Feng, X., Jiang, K., Fan, S. & Kanan, M. W. Grain-boundary-dependent CO₂ electroreduction activity. *J. Am. Chem. Soc.* **137**, 4606–4609 (2015).
- Sen, S., Liu, D. & Palmore, G. T. R. Electrochemical reduction of CO₂ at copper nanofoams. *ACS Catal.* **4**, 3091–3095 (2014).
- Lu, Q. et al. A selective and efficient electrocatalyst for carbon dioxide reduction. *Nat. Commun.* **5**, 3242 (2014).
- Jiang, K. et al. Metal ion cycling of Cu foil for selective C–C coupling in electrochemical CO₂ reduction. *Nat. Catal.* **1**, 111–119 (2018).
- Chen, Y., Li, C. W. & Kanan, M. W. Aqueous CO₂ reduction at very low overpotential on oxide-derived Au nanoparticles. *J. Am. Chem. Soc.* **134**, 19969–19972 (2012).
- Sreekanth, N. & Phanim, K. L. Selective reduction of CO₂ to formate through bicarbonate reduction on metal electrodes: new insights gained from SG/TC mode of SECM. *Chem. Commun.* **50**, 11143–11146 (2014).
- Asadi, M. et al. Robust carbon dioxide reduction on molybdenum disulphide edges. *Nat. Commun.* **5**, 4470 (2014).
- Wu, J. et al. Achieving highly efficient, selective, and stable CO₂ reduction on nitrogen-doped carbon nanotubes. *ACS Nano* **9**, 5364–5371 (2015).
- Wu, B. & Zheng, N. Surface and interface control of noble metal nanocrystals for catalytic and electrocatalytic applications. *Nano Today* **8**, 168–197 (2013).
- Raciti, D., Livi, K. J. & Wang, C. Highly dense Cu nanowires for low-overpotential CO₂ reduction. *Nano Lett.* **15**, 6829–6835 (2015).
- Zhu, W. et al. Monodisperse Au nanoparticles for selective electrocatalytic reduction of CO₂ to CO. *J. Am. Chem. Soc.* **135**, 16833–16836 (2013).
- Hall, A. S., Yoon, Y., Wuttig, A. & Surendranath, Y. Mesopore-structure-induced selectivity in CO₂ reduction catalysis. *J. Am. Chem. Soc.* **137**, 14834–14837 (2015).
- Li, C. W. & Kanan, M. W. CO₂ reduction at low overpotential on Cu electrodes resulting from the reduction of thick Cu₂O films. *J. Am. Chem. Soc.* **134**, 7231–7234 (2012).
- Mettela, G. & Kulkarni, G. U. Facet selective etching of Au microcrystallites. *Nano Res.* **8**, 2925–2934 (2015).
- Kim, D., Resasco, J., Yu, Y., Asiri, A. M. & Yang, P. Synergistic geometric and electronic effects for electrochemical reduction of carbon dioxide using gold-copper bimetallic nanoparticles. *Nat. Commun.* **5**, 4948 (2014).
- Wang, H., Chen, Y., Hou, X., Ma, C. & Tan, T. Nitrogen-doped graphenes as efficient electrocatalysts for the selective reduction of carbon dioxide to formate in aqueous solution. *Green Chem.* **18**, 3250–3256 (2016).
- Du, L. et al. Advanced catalyst supports for PEM fuel cell cathodes. *Nano Energy* **29**, 314–322 (2016).
- Verma, S., Lu, X., Ma, S., Masel, R. & Kenis, P. J. The effect of electrolyte composition on the electroreduction of CO₂ to CO on Ag based gas diffusion electrodes. *Phys. Chem. Chem. Phys.* **18**, 7075–7084 (2016).
- Haas, T., Krause, R., Weber, R., Demler, M. & Schmid, G. Technical photosynthesis involving CO₂ electrolysis and fermentation. *Nat. Catal.* **1**, 32–39 (2018).
- Gauthier, E., Duan, Q., Hellstern, T. & Benziger, J. Water flow in, through, and around the gas diffusion layer. *Fuel Cells* **12**, 835–847 (2012).
- Yu, S. et al. Study on hydrophobicity degradation of gas diffusion layer in proton exchange membrane fuel cells. *Energy Convers. Manag.* **76**, 301–306 (2013).
- Wagner, K., Tiwari, P., Swiegers, G. & Wallace, G. An electrochemical cell with Gortex-based electrodes capable of extracting pure hydrogen from highly dilute hydrogen-methane mixtures. *Energy Environ. Sci.* **11**, 172–184 (2018).
- Verma, S. et al. Insights into the low overpotential electroreduction of CO₂ to CO on a supported gold catalyst in an alkaline flow electrolyzer. *ACS Energy Lett.* **3**, 193–198 (2017).
- Park, J. et al. A review of the gas diffusion layer in proton exchange membrane fuel cells: durability and degradation. *Appl. Energy* **155**, 866–880 (2015).
- Singh, M. R., Kwon, Y., Lum, Y., Ager, J. W. III & Bell, A. T. Hydrolysis of electrolyte cations enhances the electrochemical reduction of CO₂ over Ag and Cu. *J. Am. Chem. Soc.* **138**, 13006–13012 (2016).
- Li, H. & Oloman, C. The electro-reduction of carbon dioxide in a continuous reactor. *J. Appl. Electrochem.* **35**, 955–965 (2005).
- Rosen, B. A. et al. Ionic liquid-mediated selective conversion of CO₂ to CO at low overpotentials. *Science* **334**, 643–644 (2011).
- Clark, E. L., Hahn, C., Jaramillo, T. F. & Bell, A. T. Electrochemical CO₂ reduction over compressively strained CuAg surface alloys with enhanced multi-carbon oxygenate selectivity. *J. Am. Chem. Soc.* **139**, 15848–15857 (2017).
- Weekes, D. M., Salvatore, D. A., Reyes, A., Huang, A. & Berlinguette, C. P. Electrolytic CO₂ reduction in a flow cell. *Acc. Chem. Res.* **51**, 910–918 (2018).
- Liu, M. et al. Enhanced electrocatalytic CO₂ reduction via field-induced reagent concentration. *Nature* **537**, 382–386 (2016).
- Weibel, E. R., Sapoval, B. & Filoche, M. Design of peripheral airways for efficient gas exchange. *Resp. Physiol. Neurobiol.* **148**, 3–21 (2005).
- Ionescu, C. M. in *The Human Respiratory System: An Analysis of the Interplay between Anatomy, Structure, Breathing and Fractal Dynamics* 13–22 (Springer, London, 2013).
- Arora, P. & Zhang, Z. Battery separators. *Chem. Rev.* **104**, 4419–4462 (2004).
- Ji, M. & Wei, Z. A review of water management in polymer electrolyte membrane fuel cells. *Energies* **2**, 1057–1106 (2009).
- Karimi, G., Jafarpour, F. & Li, X. Characterization of flooding and two-phase flow in polymer electrolyte membrane fuel cell stacks. *J. Power Sources* **87**, 156–164 (2009).
- Fairweather, J. D., Li, B., Mukundan, R., Fenton, J. & Borup, R. L. In situ and ex situ characterization of carbon corrosion in PEMFCs. *ECS Tran.* **3**, 433–446 (2010).
- Hiramitsu, Y., Sato, H., Kobayashi, K. & Hori, M. Controlling gas diffusion layer oxidation by homogeneous hydrophobic coating for polymer electrolyte fuel cells. *J. Power Sources* **96**, 5453–5469 (2011).
- Ha, T. et al. Experimental study of the effect of dissolution on the gas diffusion layer in polymer electrolyte membrane fuel cells. *Int. J. Hydrog. Energy* **6**, 12427–12435 (2011).
- Sheng, X. et al. Enhanced photocatalytic reaction at air-liquid-solid joint interfaces. *J. Am. Chem. Soc.* **39**, 12402–12405 (2017).
- Mariano, R. G., McKelvey, K., White, H. S. & Kanan, M. W. Selective increase in CO₂ electroreduction activity at grain-boundary surface terminations. *Science* **58**, 1187–1192 (2017).
- Bin, X., Sargent, E. H. & Kelley, S. O. Nanostructuring of sensors determines the efficiency of biomolecular capture. *Anal. Chem.* **82**, 5928–5931 (2010).
- Oyama, S. T., Went, G. T., Lewis, K. B., Bell, A. T. & Somorjai, G. A. Oxygen chemisorption and laser Raman spectroscopy of unsupported and silica-supported vanadium oxide catalysts. *J. Phys. Chem.* **93**, 6786–6790 (1989).
- Kas, R. et al. Three-dimensional porous hollow fibre copper electrodes for efficient and high-rate electrochemical carbon dioxide reduction. *Nat. Commun.* **7**, 10748 (2016).
- Suddhasatwa, B. *Recent Trends in Fuel Cell Science and Technology* (Springer, New York, 2007).
- Kopljär, D., Inan, A., Vindayer, P., Wagner, N. & Klemm, E. Electrochemical reduction of CO₂ to formate at high current density using gas diffusion electrodes. *J. Appl. Electrochem.* **44**, 1107–1116 (2014).
- Gupta, N., Gattrell, M. & MacDougall, B. Calculation for the cathode surface concentrations in the electrochemical reduction of CO₂ in KHCO₃ solutions. *J. Appl. Electrochem.* **36**, 161–172 (2006).
- Varela, A. S., Kroschel, M., Reier, T. & Strasser, P. Controlling the selectivity of CO₂ electroreduction on copper: the effect of the electrolyte concentration and the importance of the local pH. *Catal. Today* **60**, 8–13 (2016).
- Wuttig, A., Yaguchi, M., Motobayashi, K., Osawa, M. & Surendranath, Y. Inhibited proton transfer enhances Au-catalyzed CO₂-to-fuels selectivity. *Proc. Natl Acad. Sci. USA* **113**, E4585–E4593 (2016).
- Bockris, J. O. M., Conway, B. E., & White, R. E. *Modern Aspects of Electrochemistry* 89–189 (Springer Science & Business Media, New York, 2008).
- Kim, B., Ma, S., Jhong, H. R. M. & Kenis, P. J. Influence of dilute feed and pH on electrochemical reduction of CO₂ to CO on Ag in a continuous flow electrolyzer. *Electrochim. Acta* **66**, 271–276 (2015).
- Kuhl, K. P., Cave, E. R., Abram, D. N. & Jaramillo, T. F. New insights into the electrochemical reduction of carbon dioxide on metallic copper surfaces. *Energy Environ. Sci.* **5**, 7050–7059 (2012).
- Lobaccaro, P. et al. Effects of temperature and gas-liquid mass transfer on the operation of small electrochemical cells for the quantitative evaluation of CO₂ reduction electrocatalysts. *Phys. Chem. Chem. Phys.* **18**, 26777–26785 (2016).

Acknowledgements

This work was supported by the Department of Energy, Office of Basic Energy Sciences, Materials Sciences and Engineering Division under contract DEAC02-76-SF00515.

The authors acknowledge the use and support of the Stanford Nano Shared Facilities and Stanford Nanofabrication Facility. The authors thank G. Zhou, Z. Lu, W. Chen and L. Cai for helpful discussions. J.L. thanks R. Brinks Lockwood for writing suggestions.

Author contributions

J.L., S.C. and Y.C. conceived the idea for the project. J.L., Z.L., H.R.L., Y.Z. and H.W. performed the structural characterization. J.L. and Y.Z. performed the theoretical analysis. J.L., G.C, C.-L.W. and K.L. conducted the device fabrication. J.L. conducted the performance measurements and analysed the data. J.L., A.P., S.C. and Y.C. wrote the manuscript. S.C. and Y.C. supervised the project. All authors discussed the results and commented on the manuscript at all stages.

Competing interests

The authors declare no competing interests.

Additional information

Supplementary information is available for this paper at <https://doi.org/10.1038/s41929-018-0108-3>.

Reprints and permissions information is available at www.nature.com/reprints.

Correspondence and requests for materials should be addressed to Y.C.

Publisher's note: Springer Nature remains neutral with regard to jurisdictional claims in published maps and institutional affiliations.